

**Color-gradient lattice Boltzmann model for simulating droplet motion with contact-angle hysteresis**Yan Ba,<sup>1</sup> Haihu Liu,<sup>2</sup> Jinju Sun,<sup>1,\*</sup> and Rongye Zheng<sup>1</sup><sup>1</sup>*School of Energy and Power Engineering, Xi'an Jiaotong University, 28 West Xianning Road, Xi'an 710049, China*<sup>2</sup>*Department of Civil and Environmental Engineering, University of Illinois at Urbana-Champaign, Urbana, Illinois 61801, USA*

(Received 8 July 2013; published 18 October 2013)

Lattice Boltzmann method (LBM) is an effective tool for simulating the contact-line motion due to the nature of its microscopic dynamics. In contact-line motion, contact-angle hysteresis is an inherent phenomenon, but it is neglected in most existing color-gradient based LBMs. In this paper, a color-gradient based multiphase LBM is developed to simulate the contact-line motion, particularly with the hysteresis of contact angle involved. In this model, the perturbation operator based on the continuum surface force concept is introduced to model the interfacial tension, and the recoloring operator proposed by Latva-Kokko and Rothman is used to produce phase segregation and resolve the lattice pinning problem. At the solid surface, the color-conserving wetting boundary condition [Hollis *et al.*, *IMA J. Appl. Math.* **76**, 726 (2011)] is applied to improve the accuracy of simulations and suppress spurious currents at the contact line. In particular, we present a numerical algorithm to allow for the effect of the contact-angle hysteresis, in which an iterative procedure is used to determine the dynamic contact angle. Numerical simulations are conducted to verify the developed model, including the droplet partial wetting process and droplet dynamical behavior in a simple shear flow. The obtained results are compared with theoretical solutions and experimental data, indicating that the model is able to predict the equilibrium droplet shape as well as the dynamic process of partial wetting and thus permits accurate prediction of contact-line motion with the consideration of contact-angle hysteresis.

DOI: [10.1103/PhysRevE.88.043306](https://doi.org/10.1103/PhysRevE.88.043306)

PACS number(s): 47.11.-j, 47.55.Ca

**I. INTRODUCTION**

Microdroplet behavior on a solid surface is of significant importance in numerous industrial processes such as coating technique, ink-jet printers, and multiphase flows in microchannels, and has attracted the increasing attention and interest of many researchers. In microdroplet dynamics, the behavior of the contact-line region plays a crucial role, where three phases (liquid-vapor-solid or liquid-liquid-solid) coexist, and the physical mechanism is very complex because of the microscopic interactions among the fluid and solid phases [1].

In past decades, some numerical methods dealing with contact-line behavior have been proposed based on macroscopic hydrodynamic equations and/or microscopic molecular dynamics. In the commonly used macroscopic approaches, e.g., volume of fluid (VOF) [2,3] and level-set methods [4,5], the interfacial behavior is often obtained by solving a transport equation of the volume fraction (level-set function) and implementing an interface reconstruction (reinitialization) process, which is very complicated and usually difficult to be implemented. In addition, empirical slip models are required for such kinds of methods to overcome the stress singularity problem associated with the traditional no-slip boundary condition. The microscopic methods (e.g., the molecular dynamics methods, and direct simulation Monte Carlo methods) have also been applied to multiphase fluid dynamic simulations, but their requirement for the computational resources will greatly increase with the number of particles and physical time scale involved in the problems, which largely restricts their applications for practical problems [6].

Recently, the lattice Boltzmann method (LBM) has emerged as a promising approach for modeling the

microdroplet behavior [7–9]. LBM is a mesoscopic computational method between the molecular dynamics methods and the macroscopic hydrodynamic approaches. Instead of solving the macroscopic continuum equations, LBM solves the kinetic-based evolution equations of the particle distribution function that describes the averaged macroscopic behavior of the molecules, and the macroscopic variables can be calculated by the moment integrations of the distribution function. Due to its kinetic nature, LBM can automatically capture the multiphase interface, and the numerical difficulties in traditional multiphase simulations such as phase segregation and contact-line dynamics can be resolved through the incorporation of intermolecular-level interactions.

Several multiphase LBM models have been developed in past years. Shan and Chen proposed a pseudopotential model [10], in which the interparticle forces were incorporated into the equilibrium velocity to model the interfacial tension and produce phase separation. The free-energy model proposed by Swift *et al.* [11] considered a generalized equilibrium distribution function derived from the free-energy functional to model the interfacial dynamics, which can conserve the local mass and momentum, and is thermodynamically consistent for describing the interfacial dynamics. The present study is based on the color-gradient model originally proposed by Gunstensen *et al.* [12], which used the red and blue particle distribution functions to represent two different fluids. In the color-gradient model of Gunstensen *et al.*, an additional collision operator (i.e., the perturbation term) is introduced to generate the interfacial tension, and a recoloring step is applied to demix the different phases through maximizing the work done by color gradient. Despite its simplicity in physical concept and numerical implementation, Gunstensen's model suffers from a few shortcomings, such as the existence of large spurious velocities in the vicinity of the interface, and equal densities requirement for two-phase flows. Several

\*Corresponding author: [jjsun@mail.xjtu.edu.cn](mailto:jjsun@mail.xjtu.edu.cn)

modifications of the original model have been conducted to eliminate these limitations and improve its accuracy and efficiency. Latva-Kokko and Rothman [13] replaced the numerical maximization recoloring step of Gunstensen’s model through a formulaic segregation algorithm, which removes the lattice pinning problem at the interface region and meanwhile improves the computational efficiency. Lishchuk *et al.* [14] introduced the concept of continuum surface force (CSF) to model the interfacial tension, which effectively reduces the spurious velocities in the interface region. The ability of the model to allow for variations of density and viscosity was introduced by Grunau *et al.* [15] through the incorporation of the freedom of the rest particle equilibrium distribution function. Reis and Phillips [16] further developed a two-dimensional (2D) nine-velocity (D2Q9) model for immiscible fluids with larger density ratio. Recently, Liu *et al.* [17] extended the model of Reis and Philips to three-dimensional cases by deriving a generalized perturbation operator in which an expression for the interfacial tension parameter is directly obtained without any additional approximations.

In color-gradient models, the contact angle is usually considered by directly prescribing a color-function value on the wall [18–20] or implementing a color-conserving wetting boundary condition [21] in both static and dynamic contact-line simulations. For both methods used in dynamic situations, the classical Navier slip rule [22,23] in hydrodynamic models between the dynamic contact angle and contact-line velocity is naturally satisfied without introducing any assumption due to the nature of the microscopic dynamics [19], which makes the color-gradient model an effective tool for the dynamic contact-angle simulations. However, in these models, the contact-angle hysteresis behavior, which is essentially inherent to contact-line motion, has been neglected. The contact-angle hysteresis is known as a phenomenon in which the contact line remains fixed at a given position, as the instantaneous contact angle  $\theta$  is within the window of  $\theta_R < \theta < \theta_A$ , where  $\theta_R$  and  $\theta_A$  are the limited values for the receding and advancing contact angles. Generally, the hysteresis window is determined by the properties of the solid substrates in contact with the droplet such as surface roughness and nonuniformity [24,25], which is complicated and has not been fully understood. In numerical simulations, we focus mainly on the droplet behavior with a given hysteresis window. The difficulties in numerical modeling of the contact-angle hysteresis for a given hysteresis window mainly lies in the determination of an instantaneous

dynamic contact angle  $\theta_d$  that satisfies the following condition: the droplet only deforms naturally within the interval  $(\theta_R, \theta_A)$ , beyond which it will move on the solid surface with  $\theta_d$  obeying the Navier slip rule. Several numerical strategies based on macroscopic multiphase methods have been developed to simulate the contact-angle hysteresis behavior. For instance, in the level-set method a feedback deceleration technique is developed by Park *et al.* [26] to simulate the moving contact-line behavior. Dupont *et al.* [27] proposed a VOF-based multiphase model to simulate the hysteresis behavior, in which an iterative method is used to update the equilibrium contact angle according to the momentum balance, and the dynamic contact angle is determined by the updated equilibrium contact angle. The above-mentioned numerical strategies are restricted to the macroscopic Navier-Stokes-based multiphase models, and some efforts and attempts are urgently required to model the contact-angle hysteresis in the LBMs with their increasing popularity.

In the present study, a dynamic contact-angle model including hysteresis is developed based on the color-gradient multiphase LBM model. A perturbation operator based on the CSF concept is used to model the interfacial tension, and the recoloring operator originally proposed in Ref. [13] is introduced to maintain the interface between two fluids. At the solid surface, the color-conserving wetting boundary condition [21] is incorporated into the model to describe the dynamic evolution of the contact line, and a modified numerical strategy previously used in the VOF-based model [27] is developed to account for the contact-angle hysteresis. The capability and accuracy of the proposed model are tested by several typical flow cases, including the droplet partial wetting process, and the dynamic behavior of a droplet subjected to a simple shear flow.

## II. MATHEMATICAL MODEL

### A. Lattice Boltzmann immiscible two-phase model

The two-dimensional color-gradient model is developed for immiscible two-phase fluids based on work by Halliday *et al.* [28] and Reis *et al.* [16]. In the model, two immiscible fluids are represented as a red fluid and a blue fluid, respectively. The distribution function for each fluid is denoted by  $f_{i,k}$ , where  $k = \text{red or blue}$ ,  $i = 0, \dots, 8$  is velocity directions for a D2Q9 lattice grid, and the total distribution function is defined as  $f_i = f_{i,R} + f_{i,B}$ . The lattice velocity vectors on the D2Q9 grid are given as

$$\mathbf{c}_i = \begin{cases} (0, 0), & i = 0 \\ (\cos[\pi(i-1)/2], \sin[\pi(i-1)/2]), & i = 1, 2, 3, 4 \\ \sqrt{2}(\cos[\pi(i-5)/2 + \pi/4], \sin[\pi(i-5)/2 + \pi/4]), & i = 5, 6, 7, 8. \end{cases} \quad (1)$$

In each time step, the distribution function of each fluid undergoes a collision substep and a streaming substep, and the evolution equation is expressed by

$$f_{i,k}(\mathbf{x} + \mathbf{c}_i \delta_t, t + \delta_t) = f_{i,k}(\mathbf{x}, t) + \Omega_{i,k}[f_{i,k}(\mathbf{x}, t)], \quad (2)$$

where  $\mathbf{x}$  and  $t$  are the position and time,  $\delta_t$  is the time step, and  $\Omega_{i,k}$  is the collision operator. The collision operator  $\Omega_{i,k}$  consists of three separate parts [16]:

$$\Omega_{i,k} = (\Omega_{i,k})^{(3)}[(\Omega_{i,k})^{(1)} + (\Omega_{i,k})^{(2)}], \quad (3)$$

where  $(\Omega_{i,k})^{(1)}$  is the Bhatnagar-Gross-Krook (BGK) collision operator,  $(\Omega_{i,k})^{(2)}$  is the perturbation operator which generates an interfacial tension, and  $(\Omega_{i,k})^{(3)}$  is the recoloring operator which contributes to maintaining the phase interface.

For each phase, mass conservation and total momentum conservation are expressed as

$$\begin{aligned}\rho_k &= \sum_i f_{i,k} = \sum_i f_{i,k}^{(\text{eq})}, \\ \rho \mathbf{u} &= \sum_i \sum_k \mathbf{c}_i f_{i,k} = \sum_i \sum_k \mathbf{c}_i f_{i,k}^{(\text{eq})},\end{aligned}\quad (4)$$

where  $\rho_k$  is the density of fluid  $k$ ,  $\rho = \rho_R + \rho_B$  is the total density, and  $\mathbf{u}$  is the velocity of the fluid mixture.

### 1. BGK collision operator

In the present study, the BGK collision operator is applied for each fluid, of which the particle distribution functions are relaxed toward a local equilibrium with a single relaxation time, written as

$$(\Omega_{i,k})^{(1)} = -\omega_k [f_{i,k} - f_{i,k}^{(\text{eq})}]. \quad (5)$$

For a given multiphase flow, the equilibrium distribution function is defined by [16]

$$f_{i,k}^{(\text{eq})}(\rho, \mathbf{u}) = \rho_k (\phi_{i,k} + W_i [3\mathbf{c}_i \cdot \mathbf{u} + 4.5(\mathbf{c}_i \cdot \mathbf{u})^2 - 1.5(\mathbf{u}^2)]), \quad (6)$$

where  $W_i$  is the weight defined as

$$W_i = \begin{cases} 4/9, & i = 0 \\ 1/9, & i = 1, 2, 3, 4 \\ 1/36, & i = 5, 6, 7, 8, \end{cases} \quad (7)$$

and  $\phi_{i,k}$  is a parameter related to the density ratio written as [16]

$$\phi_{i,k} = \begin{cases} \alpha_k, & i = 0 \\ (1 - \alpha_k)/5, & i = 1, 2, 3, 4 \\ (1 - \alpha_k)/20, & i = 5, 6, 7, 8, \end{cases} \quad (8)$$

where  $0 \leq \alpha_k \leq 1$  should be satisfied to avoid the unreal negative value for fluid density. Note that  $\alpha_R$  and  $\alpha_B$  should satisfy the constraint  $\gamma = \rho_R/\rho_B = (1 - \alpha_B)/(1 - \alpha_R)$  [16,17], where  $\gamma$  is the density ratio of red fluid to blue fluid. The present model has been proved to be valid under different density ratios [15,16]. For example, in Ref. [16], simulations of density ratio up to 18.5 were presented. But since our concern is to model the contact-angle hysteresis, we only choose  $\gamma = 1$  in this work for the sake of simplicity.

The interface between the two phases is identified by the constant contours of the phase field function  $\rho^N$ , which is defined as

$$\rho^N(\mathbf{x}, t) = \frac{\rho_R(\mathbf{x}, t) - \rho_B(\mathbf{x}, t)}{\rho_R(\mathbf{x}, t) + \rho_B(\mathbf{x}, t)}. \quad (9)$$

In the single-phase regions ( $|\rho^N|=1$ ), the Chapman-Enskog expansion is employed for each phase by which the Navier-Stokes equations are recovered. The relaxation parameter  $\omega_k$  is a function of fluid kinematic viscosity and given by  $\omega_k = 1/(3\nu_k + 0.5)$  [17], in which  $\nu_k$  is the kinematic viscosity of fluid  $k$ .

In the interface region ( $|\rho^N| < 1$ ), to ensure the smoothness of the relaxation parameter and the stability of the interface, the relaxation parameter is written as [16]

$$\omega = \begin{cases} \omega_R, & \rho^N > \delta \\ g_R(\rho^N), & \delta \geq \rho^N > 0 \\ g_B(\rho^N), & 0 \geq \rho^N > -\delta \\ \omega_B, & \rho^N < -\delta, \end{cases} \quad (10)$$

where  $\delta$  is a free parameter associated with the interface thickness and taken as 0.1 in the present simulation, and  $g_R$  and  $g_B$  are parabolic functions of  $\rho^N$  written as

$$\begin{aligned}g_R(\rho^N) &= \chi + \eta\rho^N + \kappa(\rho^N)^2, \\ g_B(\rho^N) &= \chi + \lambda\rho^N + \nu(\rho^N)^2\end{aligned}\quad (11)$$

in which the coefficients are taken as

$$\begin{aligned}\chi &= 2\omega_R\omega_B/(\omega_R + \omega_B), \\ \eta &= 2(\omega_R - \chi)/\delta, \\ \kappa &= -\eta/(2\delta), \\ \lambda &= 2(\chi - \omega_B)/\delta, \\ \nu &= \lambda/(2\delta).\end{aligned}\quad (12)$$

### 2. Perturbation operator

In the perturbation operator, the CSF model [28] is used to model the interfacial tension, which has been demonstrated to effectively reduce the spurious velocities [14]. The interface force acts centripetally normal to the local interface and its magnitude is proportional to the gradient of the phase field function (i.e., color gradient)  $\nabla\rho^N$ . The local curvature of the interface is given by

$$K = -\nabla_S \cdot \mathbf{n}, \quad (13)$$

where  $\nabla_S = (\mathbf{I} - \mathbf{nn}) \cdot \nabla$  is the surface gradient operator and  $\mathbf{n} = -\nabla\rho^N/|\nabla\rho^N|$  is the outward-pointing unit normal vector of the interface. In two dimensions, the curvature of the interface can be expressed by

$$K = n_x n_y \left( \frac{\partial}{\partial y} n_x + \frac{\partial}{\partial x} n_y \right) - n_x^2 \frac{\partial}{\partial y} n_y - n_y^2 \frac{\partial}{\partial x} n_x. \quad (14)$$

To minimize the discretization errors, the derivatives in Eq. (14) are calculated numerically through the nine-point isotropic finite difference approximation for a variable  $\psi$ ,

$$\nabla\psi(\mathbf{x}, t) = 3 \sum_i w_i \mathbf{c}_i \psi(\mathbf{x} + \mathbf{c}_i, t). \quad (15)$$

The interfacial tension force is then obtained by

$$\mathbf{F} = -\frac{1}{2}\sigma K \nabla\rho^N, \quad (16)$$

where  $\sigma$  is the interfacial tension which is applied only at the lattice sites where the two fluids coexist.

The interfacial tension force can be incorporated into LBM using different models. In the present study, the body force model of Guo *et al.* [29] is employed for its high accuracy in modeling a spatially varying body force and capability in reducing effectively the spurious velocities. According to

Guo *et al.*, the perturbation operator  $(\Omega_i)^{(2)} = (\Omega_{i,R})^{(2)} + (\Omega_{i,B})^{(2)}$  is written as

$$(\Omega_i)^{(2)} = W_i \left(1 - \frac{w}{2}\right) [3(\mathbf{c}_i - \mathbf{u}) + 9(\mathbf{c}_i \cdot \mathbf{u})] \cdot \mathbf{F}, \quad (17)$$

where the velocity is redefined to include some of the effect of external body force

$$\rho \mathbf{u} = \sum_i \sum_k \mathbf{c}_i f_{i,k} + \frac{1}{2} \mathbf{F}. \quad (18)$$

Then the interfacial tension contribution is assigned to each phase, and the perturbation operator of fluid  $k$  is given by

$$(\Omega_{i,k})^{(2)} = A_k W_i \left(1 - \frac{w}{2}\right) [3(\mathbf{c}_i - \mathbf{u}) + 9(\mathbf{c}_i \cdot \mathbf{u}) \mathbf{c}_i] \cdot \mathbf{F}, \quad (19)$$

where  $A_k$  is the fraction of interfacial tension contributed by the fluid  $k$ , and satisfies  $\sum_k A_k = 1$ .

### 3. Recoloring operator

In this work, the recoloring algorithm proposed by Latva-Kokko and Rothman [13] is used to promote phase segregation and to maintain a reasonable interface. This algorithm allows the red and blue fluids to mix moderately at the tangent of the interface, and at the same time keeps the color distribution symmetric with respect to the color gradient. Thus, it can further reduce the spurious velocities and remove the lattice pinning problem produced by the original recoloring operator of Gunstensen *et al.* [12]. The algorithm is written as

$$\begin{aligned} (\Omega_{i,R})^{(3)}(f_{i,R}) &= \frac{\rho_R}{\rho} f'_i + \beta \frac{\rho_R \rho_B}{\rho^2} \\ &\quad \times \cos(\varphi_i) |\mathbf{c}_i| \sum_k f_{i,k}^{(\text{eq})}(\rho_k, 0, \alpha_k), \\ (\Omega_{i,B})^{(3)}(f_{i,B}) &= \frac{\rho_B}{\rho} f'_i - \beta \frac{\rho_R \rho_B}{\rho^2} \\ &\quad \times \cos(\varphi_i) |\mathbf{c}_i| \sum_k f_{i,k}^{(\text{eq})}(\rho_k, 0, \alpha_k), \end{aligned} \quad (20)$$

where  $f'_i$  is the post-perturbation value of the total distribution function;  $\varphi_i$  is the angle between the color gradient  $\nabla \rho^N$  and the lattice direction  $\mathbf{c}_i$ ; and  $\beta$  is a free parameter associated with the interface thickness and takes a value between zero and unity. In this study,  $\beta$  is taken as 0.7 to maintain a steady interface [28], which has a thickness of four to five lattices. In addition, a previous study also showed that this choice is necessary to reproduce correct droplet dynamics [20].

### B. Numerical implementation of wetting boundary condition

The physical mechanism for microdroplet motion on a solid surface remains poorly understood mainly due to the complexity of the contact-line dynamics. In this section, we aim to develop a color-gradient wetting boundary condition that allows one to achieve accurate simulation of the contact-line dynamics including hysteresis. To achieve this goal, a color-conserving scheme [21] is employed at the wetting boundary to model the dynamics of the contact line with improved accuracy and minimized spurious velocities. In addition, the contact-angle hysteresis is included by an iterative

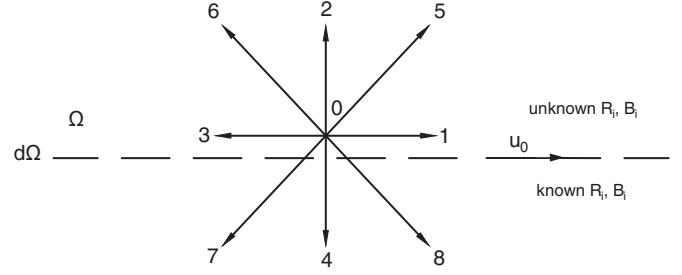


FIG. 1. Illustration of a D2Q9 lattice node on the bottom boundary of a 2D domain (at propagation step).

algorithm based on the numerical strategy of Dupont and Legendre [27], but some modifications are introduced since the original model of Dupont and Legendre is designated for the macroscopic VOF-based methods.

#### 1. Color-conserving boundary condition

To model the fluid-surface interactions, we employ the color-conserving wetting boundary condition proposed by Hollis *et al.* [21] with some modifications according to our collision operator  $\Omega_{i,k}$ , in which the boundary closure scheme is applied to ensure the mass conservation for each phase, and a variant of the recoloring operator is designed to maintain the reasonable interface at the solid boundary.

Figure 1 represents a lattice node on the bottom wall, which moves at the velocity of  $\mathbf{u}_0 = (u_{0,x}, u_{0,y})$ . Assume that the node just lies in the interface of the red and blue fluids. At this lattice node, the post-propagation value of fluid distribution function  $f_{i,k}$  exists only for  $i \neq 2, 5, 6$ , thus, the total distribution function that propagates into the fluid domain at the node for each phase is written as  $F_{\text{in}}^k = \sum_{i \neq 2, 5, 6} f_{i,k}$ . On the other hand, the post-perturbation value of the distribution function  $f'_{i,k}$  needs to be considered only for live links, i.e.,  $i \neq 4, 7, 8$ , since the post-perturbation distribution functions with  $i = 4, 7, 8$  will propagate out of the fluid domain. Therefore, the effective mass for each phase after collision is given as  $\sum_{i \neq 4, 7, 8} f'_{i,k}$ . To ensure mass conservation for each phase, the post-propagation and post-perturbation effective mass of each phase must be equal. Thus, the color conservation can then be expressed as

$$F_{\text{in}}^k = \sum_{i \neq 4, 7, 8} f'_{i,k}. \quad (21)$$

According to the lattice Boltzmann equation, i.e., Eq. (2), the distribution function of each phase after the collision can be written as

$$f'_{i,k} = f_{i,k}^{(0)}(\rho'_k, \mathbf{u}_0) + (\Omega_{i,k})^{(2)} + (1 - \omega) f_{i,k}^{(1)}, \quad (22)$$

where  $\rho'_k$  represents the auxiliary boundary density determined by the color conservation. The subtotal of the higher-order component of the distribution functions  $f_{i,k}^{(1)}$  on the live links is assumed to be zero, and the subtotal of the perturbation operator  $(\Omega_{i,k})^{(2)}$  [defined by Eq. (19)] on the live links disrupts the conservation by

$$\begin{aligned} \Delta M_k &= \sum_{i \neq 4, 7, 8} (\Omega_{i,k})^{(2)} = \sum_{i \neq 4, 7, 8} A_k W_i \left(1 - \frac{w}{2}\right) \\ &\quad \times [3(\mathbf{c}_i - \mathbf{u}_0) + 9(\mathbf{c}_i \cdot \mathbf{u}_0) \mathbf{c}_i] \cdot \mathbf{F} \neq 0. \end{aligned} \quad (23)$$

Thus, the subtotal of the equilibrium distribution function  $f_{i,k}^{(0)}(\rho'_k, \mathbf{u}_0)$  can be derived using Eq. (22), and written as

$$F_{\text{in}}^k - \Delta M_k = \sum_{i \neq 4,7,8} f_{i,k}^{(0)}(\rho'_k, \mathbf{u}_0). \quad (24)$$

Then, the auxiliary boundary density  $\rho'_k$  is obtained by introducing the equilibrium distribution function into the above equation:

$$\rho'_k = \frac{F_{\text{in}}^k - \Delta M_k}{\sum_{i \neq 4,7,8} f_{i,k}^{(0)}(\mathbf{1}, \mathbf{u}_0)} = \frac{F_{\text{in}}^k - \Delta M_k}{(0.7 + 0.3\alpha_k + 0.5u_{0y} - 0.5u_{0y}^2)}. \quad (25)$$

In the present study, the  $y$  component of wall velocity is zero, i.e.,  $u_{0y} = 0$ , and thus we get

$$\rho'_k = \frac{F_{\text{in}}^k - \Delta M_k}{0.7 + 0.3\alpha_k}. \quad (26)$$

The higher-order distribution function  $f_{i,k}^{(1)}$  should satisfy the following constraints as given in Ref. [21]:

$$\begin{aligned} \sum_{i \neq 4,7,8} f_{i,k}^{(1)} &= 0, \\ \sum_i f_{i,k}^{(1)} c_{i\alpha} &= \frac{1}{2} F_{\alpha}, \\ \sum_i f_{i,k}^{(1)} c_{i\alpha} c_{i\beta} &= -\frac{2}{3} \rho'_k S_{\alpha\beta} / w, \end{aligned} \quad (27)$$

where  $S_{\alpha\beta}$  is the strain rate tensor and defined as [21]

$$S_{\alpha\beta} = \frac{1}{2} (\partial_\alpha u_\beta + \partial_\beta u_\alpha) + \frac{3w}{4\rho} (F_\alpha u_\beta + F_\beta u_\alpha). \quad (28)$$

Solving the underspecified Eq. (27) (because the number of unknowns is more than the number of equations) by the singular value decomposition (SVD) method [30], we obtain  $f_{i,k}^{(1)}$  as follows:

$$\begin{pmatrix} f_{0,k}^{(1)} \\ f_{1,k}^{(1)} \\ f_{2,k}^{(1)} \\ f_{3,k}^{(1)} \\ f_{5,k}^{(1)} \\ f_{6,k}^{(1)} \end{pmatrix} = \frac{1}{36} \begin{pmatrix} 0 & -5 & -12 & -2 & 0 \\ 3 & -2 & 6 & -8 & 0 \\ 0 & 1 & -12 & 10 & 0 \\ -3 & -2 & 6 & -8 & 0 \\ 3 & 4 & 6 & 4 & 9 \\ -3 & 4 & 6 & 4 & -9 \end{pmatrix} \times \begin{pmatrix} \delta_t F_x \\ \delta_t F_y \\ -2\rho'_k S_{xx} / (3w) \\ -2\rho'_k S_{yy} / (3w) \\ -2\rho'_k S_{xy} / (3w) \end{pmatrix}. \quad (29)$$

Then, the post-perturbation distribution function of each phase on the boundary can be obtained by Eq. (22).

A modified recoloring step is needed for the boundary nodes to maintain the interface after the collision process. Based on the color conservation, the post-segregation densities assigned

to the live links should satisfy

$$\sum_{i \neq 4,7,8} R_i = F_{\text{in}}^R, \quad \sum_{i \neq 4,7,8} B_i = F_{\text{in}}^B, \quad \sum_{i \neq 4,7,8} f_i = F_{\text{in}}^R + F_{\text{in}}^B, \quad (30)$$

where  $R_i$  ( $B_i$ ) represent the post-segregation distribution function of red (blue) fluid.

We define  $\rho_R$  and  $\rho_B$  as the densities of red and blue fluids at the boundary nodes, and  $\rho = \rho_R + \rho_B$  as the total density. To obtain an equation of  $\rho_R$  and  $\rho_B$ , we substitute Eq. (20) into Eq. (30) and have

$$\begin{aligned} \frac{\rho_R}{\rho_R + \rho_B} (F_{\text{in}}^R + F_{\text{in}}^B) + \beta \frac{\rho_R \rho_B}{(\rho_R + \rho_B)^2} \mathbf{n} \\ \cdot \left( \sum_{i \neq 4,7,8} \{ [R_i^{\text{eq}}(R', 0, \alpha_R) + B_i^{\text{eq}}(B', 0, \alpha_B)] \mathbf{c}_i \} \right) |\mathbf{c}_i| = F_{\text{in}}^R, \end{aligned} \quad (31)$$

which can be further written as

$$\begin{aligned} \frac{\rho_R}{\rho_R + \rho_B} (F_{\text{in}}^R + F_{\text{in}}^B) + \beta \frac{\rho_R \rho_B}{(\rho_R + \rho_B)^2} n_y \\ \times \{0.3 [\rho_R(1 - \alpha_R) + \rho_B(1 - \alpha_B)]\} = F_{\text{in}}^R, \end{aligned} \quad (32)$$

where  $n_y$  is the  $y$  component of the interface normal vector  $\mathbf{n}$ . The conservation of total mass requires

$$\rho = \sum_k \rho'_k. \quad (33)$$

Combining Eqs. (32) and (33), we obtain a cubic equation with respect to  $\rho_R$ :

$$\begin{aligned} k(\alpha_R - \alpha_B) \rho_R^3 + k(-\alpha_R + 2\alpha_B - 1) \rho_R^2 \\ + [(F_{\text{in}}^R + F_{\text{in}}^B) \rho + k\rho^2(1 - \alpha_B)] \rho_R - F_{\text{in}}^R \rho^2 = 0, \end{aligned} \quad (34)$$

where  $k = 0.3\beta n_y$ . Equation (34) can be solved by an iterative method, e.g., the Newton-Raphson method, and  $R_i$  can then be calculated using the following segregation formula:

$$\begin{aligned} R_i = \frac{\rho_R}{\rho_R + \rho_B} (f'_i) + \beta \frac{\rho_R \rho_B}{(\rho_R + \rho_B)^2} \cos(\varphi_i) |\mathbf{c}_i| \\ \times [R_i^{\text{eq}}(\rho_R, 0, \alpha_R) + B_i^{\text{eq}}(\rho_B, 0, \alpha_B)]. \end{aligned} \quad (35)$$

## 2. Numerical implementation of constant contact angle

The gradient of the phase field at the boundary nodes is calculated differently from the interior fluid nodes due to the lack of information of their adjacent nodes and the necessity for introducing the contact angle. Without losing generality, we choose a bottom boundary node to illustrate its calculation procedure.

For a specified contact angle  $\theta$ , the gradient of phase field  $\nabla \rho^N$  at the boundary node should satisfy

$$\frac{\nabla \rho^N}{|\nabla \rho^N|} = \mathbf{n} = \begin{cases} \sin \theta \mathbf{e}_x + \cos \theta \mathbf{e}_y, & \text{if } \frac{\partial \rho^N}{\partial x} < 0 \\ -\sin \theta \mathbf{e}_x + \cos \theta \mathbf{e}_y, & \text{if } \frac{\partial \rho^N}{\partial x} > 0. \end{cases} \quad (36)$$

Then, we can obtain a relation for  $x$  and  $y$  components of  $\nabla\rho^N$ :

$$\left(\frac{\partial\rho^N}{\partial y}\right)_{x,1} \sin\theta = -\left|\frac{\partial\rho^N}{\partial x}\right|_{x,1} \cos\theta. \quad (37)$$

In our present algorithm,  $(\partial\rho^N/\partial x)_{x,1}$  is determined by the central difference scheme

$$\left(\frac{\partial\rho^N}{\partial x}\right)_{x,1} = [(\rho^N)_{x+1,1} - (\rho^N)_{x-1,1}]/2. \quad (38)$$

The value of  $(\partial\rho^N/\partial y)$  is then obtained using Eq. (37). Thus, the specified contact angle is implicitly imposed by the gradient of phase field.

### 3. Implementation of dynamic contact angle

As mentioned in Sec. I, in most previously reported color-gradient models, the hysteresis of the contact line has not yet been considered. In order to reproduce the droplet behavior correctly, it is necessary to develop a contact-angle hysteresis model. Based on the numerical strategy previously proposed in a macroscopic VOF model [27], we present a color-gradient-based algorithm to account for the contact-angle hysteresis, in which an iterative procedure is incorporated to obtain an equilibrium contact angle, and the dynamic contact angle is determined by the updated equilibrium contact angle.

Generally, the hysteresis phenomenon of contact line can be defined as follows [31]:

$$\begin{aligned} U_{cl} > 0 & \text{ if } \theta_d = \theta_A, \\ U_{cl} < 0 & \text{ if } \theta_d = \theta_R, \\ U_{cl} = 0 & \text{ if } \theta_R < \theta_d < \theta_A, \end{aligned} \quad (39)$$

where  $\theta_d$  is the dynamic contact angle, and  $\theta_R$  and  $\theta_A$  are, respectively, the limited values of the receding and advancing contact angle. The hysteresis window  $(\theta_R, \theta_A)$  is determined by the properties of the solid substrates in contact with the droplet such as surface roughness and nonuniformity [24,25]. In the present simulation, we focus on the droplet behavior with a given hysteresis window. For a given hysteresis window, to model the contact-angle hysteresis behavior, at each time step, we need to obtain an instantaneous dynamic contact angle  $\theta_d$  that satisfies the following condition: the droplet deforms properly within the interval  $(\theta_R, \theta_A)$ , beyond which the droplet will move on the solid surface with  $\theta_d$  obeying the Navier slip relationship.

To achieve this goal, we first implement an iterative procedure (e.g., bisection method) for the contact-line nodes at both receding and advancing sides to find the equilibrium contact angle  $\theta_e$ , at which the  $x$  component of the fluid momentum  $u_x$  will be canceled locally, i.e.,  $u_x(\theta_e) = 0$ .

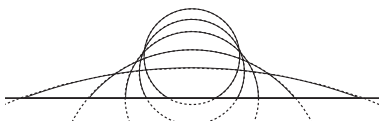


FIG. 2. Equilibrium droplet shapes for  $\theta_s = 20^\circ, 50^\circ, 90^\circ, 120^\circ, 150^\circ$ . Dashed lines: theoretical shapes. Solid lines: equilibrium shapes by the present LBM.

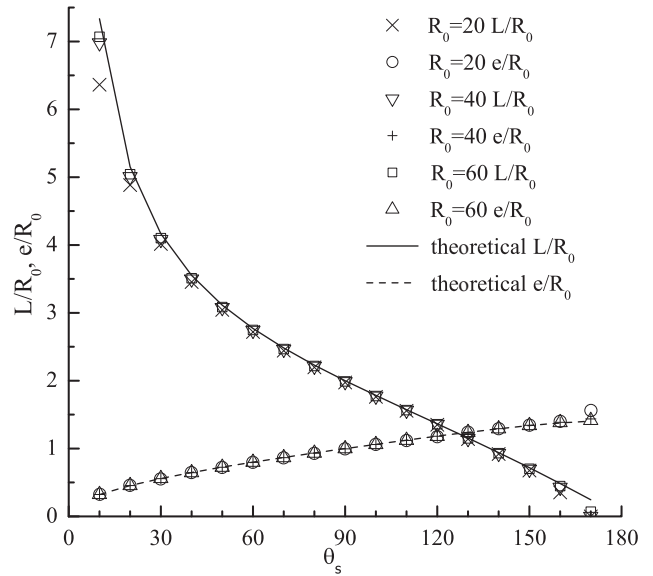


FIG. 3. Dimensionless wet length  $L/R_0$  and height  $e/R_0$  of the droplet at equilibrium as a function of the static contact angle  $\theta_s$  at different grid resolutions.

Specifically, the algorithm of finding  $\theta_e$  can be described as follows:

- (1) Give an initial range of equilibrium contact angle,  $(\theta_{\min}, \theta_{\max})$ , which is chosen to satisfy  $u_x(\theta_{\min})u_x(\theta_{\max}) \leq 0$ .
- (2) Set  $\theta_e = (\theta_{\min} + \theta_{\max})/2$  and calculate  $u_x(\theta_e)$ . If  $u_x(\theta_{\min})u_x(\theta_e) \leq 0$ , then we take  $\theta_{\max} = \theta_e$ ; otherwise, we take  $\theta_{\min} = \theta_e$ .
- (3) Repeat step 2 until the solution  $\theta_e$  satisfies the given convergence condition, e.g.,  $|u_x(\theta_e)| < 10^{-10}$ .

Subsequently, the dynamic contact angle  $\theta_d$  is determined by the following rules based on the calculated equilibrium contact angle:

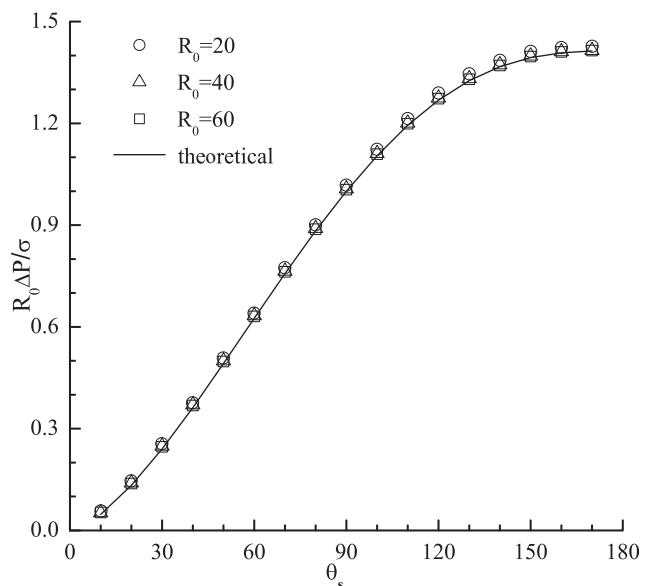


FIG. 4. Dimensionless pressure difference  $R_0\Delta P/\sigma$  of the droplet at equilibrium as a function of the static contact angle  $\theta_s$  at different grid resolutions.

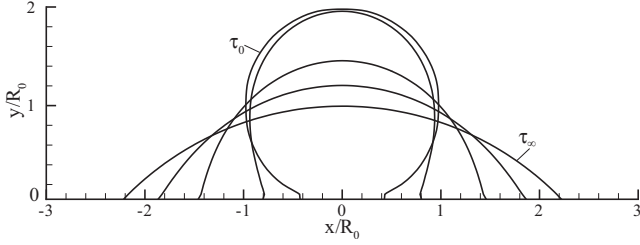


FIG. 5. Evolution of droplet shape. Time  $\tau_0$ : initial shape. Time  $\tau_\infty$ : equilibrium shape. Dimensionless time is taken as  $\tau = 0, 4.2, 14.1, 28.8, \text{ and } 1700$ .

(1) If  $\theta_R < \theta_e < \theta_A$ , the dynamic contact angle  $\theta_d$  is directly assigned as  $\theta_d = \theta_e$ , and  $\theta_d$  is then used to calculate the derivatives of the phase field at the solid wall. Thus, the momentum is locally canceled, and the contact line remains stationary on the solid wall.

(2) If  $\theta_e < \theta_R$  or  $\theta_e > \theta_A$ , the equilibrium is disrupted and the droplet starts to move over the solid surface. The dynamic contact angle  $\theta_d$  is determined such that it satisfies the well-known Navier slip relationship [23], i.e.,

$$\begin{aligned} \cos \theta_r &= \cos \theta_R + 9 \text{Ca}_{cl} \ln(r/l_m) & \text{for } \theta_e < \theta_R, \\ \cos \theta_a &= \cos \theta_A + 9 \text{Ca}_{cl} \ln(r/l_m) & \text{for } \theta_e > \theta_A, \end{aligned} \quad (40)$$

where  $\theta_r$  ( $\theta_a$ ) is the obtained dynamic contact angle at receding (advancing) side,  $\text{Ca}_{cl}$  is the contact line Capillary number defined by  $\text{Ca}_{cl} = \mu_R U_{cl} / \sigma$ ,  $r$  is the intermediate length scale, and  $l_m$  is the microscopic length scale. To guarantee the slip relationship, i.e., Eq. (40), empirical slip-length models are usually required in macroscopic models [27]. However, previous numerical simulations [19] in color-gradient models show that, the Navier slip relationship is naturally satisfied due to the nature of intermolecular interactions of LBM when the  $\theta_R$  (or  $\theta_A$ ) is appointed as the dynamic contact angle  $\theta_d$ . Based on this argument, we can simply take  $\theta_d$  as  $\theta_R$  (or  $\theta_A$ ) when  $\theta_e$  is beyond the hysteresis window, and the obtained  $\theta_d$  in simulation will vary automatically with  $\text{Ca}_{cl}$  according to Eq. (40). Therefore, no additional models or assumptions

are required in our implementation, leading to greater ease in modeling hysteresis.

Following the above-mentioned method, the real contact-line motion can be described naturally: For the equilibrium contact angle within  $(\theta_R, \theta_A)$ , it remains stationary on the solid surface, i.e., the hysteresis of contact line is exhibited; whereas for the equilibrium angle beyond the range of  $(\theta_R, \theta_A)$ , it will move.

### III. NUMERICAL RESULTS AND DISCUSSIONS

To verify the accuracy and applicability of the developed multiphase LBM, typical simulations of the contact-line motion are performed, including the droplet partial wetting process and the droplet behavior subjected to a simple shear flow, and the obtained results are compared with the experimental data and previous numerical results.

#### A. Partial wetting of the droplet

##### 1. Equilibrium shape of the droplet partial wetting

First, we investigate the equilibrium shapes of the droplet wetting on the solid surface to verify the model's ability to impose a given static contact angle  $\theta_s$ . Periodic boundary conditions are used at the left and right sides of the domain, and the bounce-back boundary condition is used at the top surface. At the bottom surface, the color-conserving wetting boundary condition is applied with the given static contact angle. The physical properties of both fluids are  $\sigma = 0.004$ ,  $\rho_R = \rho_B = 1$ , and  $\nu_R = \nu_B = 0.1$ . Different values of  $\theta_s$  are considered, ranging from  $\theta_s = 10^\circ$  to  $\theta_s = 170^\circ$ . Initially, a semicircular droplet with radius  $R_0$  is located at the center of the bottom wall, and the simulations are performed in a  $8R_0 \times 2R_0$  lattice domain with three different grid resolutions, i.e.,  $R_0 = 20$ ,  $R_0 = 40$ , and  $R_0 = 60$ , to check the grid dependence of numerical results.

Figure 2 shows the comparison between the simulated equilibrium droplet shape with its theoretical shape for the grid resolution of  $R_0 = 40$ , in which the droplet shape is represented by the contour of  $\rho^N = 0$ . It is clearly seen that

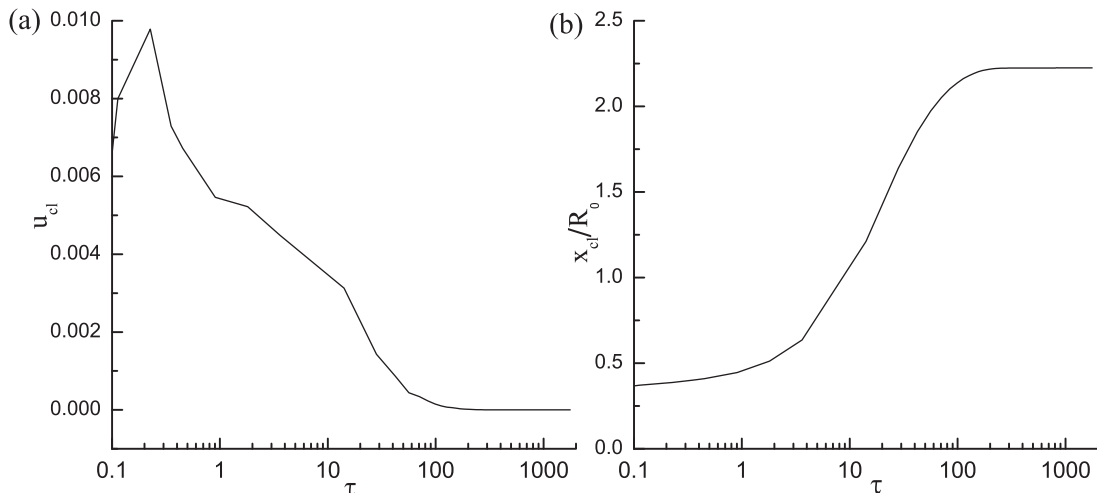


FIG. 6. Time evolution of (a) the contact-line velocity  $u_{cl}$  and (b) the advancing contact point position  $x_{cl}$ .

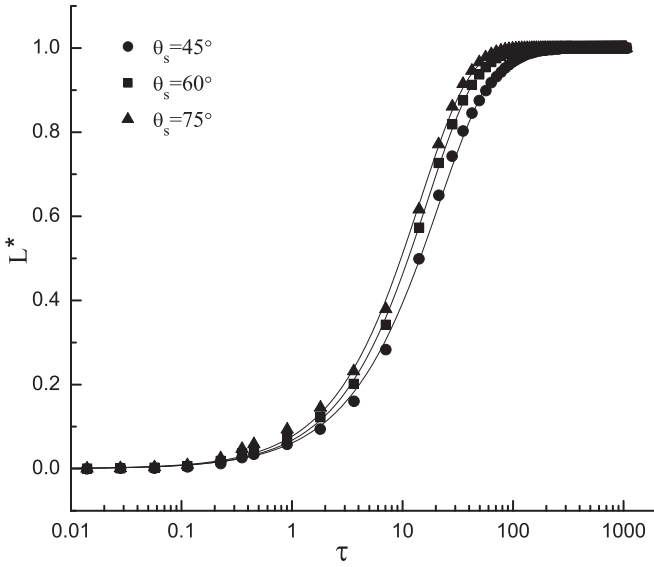


FIG. 7. The dimensionless wet length  $L^*$  as a function of the dimensionless time  $\tau$ .

good agreement is obtained for all presented contact angles. Figure 3 plots the dimensionless wet length  $L/R_0$  and height  $e/R_0$  of the droplet at the equilibrium as a function of  $\theta_s$  for different grid resolutions. The predicted wet length and height of the droplet agree well with their corresponding theoretical values at moderate contact angles for all grids, which means that even for a relatively coarse grid, our LBM simulation can predict the contact-line behavior with good accuracy. However, for extremely small and large contact angles, the wet length error is relatively large on coarse grid, and tends to decrease with increasing the grid resolution. For example, at  $\theta_s = 10^\circ$ , an error of 13.23% for wet length is found for  $R_0 = 20$ , while the error reduces to much smaller values, i.e., 4.83% for  $R_0 = 40$  and 3.60% for  $R_0 = 60$ . Figure 4 presents the dimensionless pressure difference  $R_0\Delta P/\sigma$  of the droplet at equilibrium versus the static contact angle  $\theta_s$ , in which the pressure difference is calculated from the average pressure inside the droplet ( $\rho^N \geq 0.999$ ) and outside the droplet ( $\rho^N \leq -0.999$ ). By comparing the simulated results with the theoretical solutions, good agreement is found over the entire contact-angle range for all grid resolutions.

## 2. Dynamics of partial wetting

Next, the dynamic color-conserving wetting boundary condition is validated by simulating the dynamical partial wetting process. The numerical simulation is conducted for

a droplet placed on the bottom wall in a  $160 \times 40$  lattice domain. Initially, the droplet has a radius of  $R_0 = 20$ , and its centroid is located at  $0.95R_0$  above the bottom wall. The physical properties of both fluids are  $\sigma = 0.0156$ ,  $\rho_R = \rho_B = 1$ , and  $\nu_R = \nu_B = 0.125$ . The dimensionless time  $\tau$  is used to characterize the spreading process, and is defined as  $\tau = t\sigma/(\rho\nu A^{1/2})$ , where  $A$  is the droplet area in 2D cases. Periodic boundary conditions are used at the left and right boundaries. The bounce-back boundary condition is used at the top surface, while the dynamic color-conserving wetting boundary condition is applied at the bottom surface.

Figure 5 presents the time evolution of the droplet shape for  $\theta_s = 45^\circ$ . As shown in the figure, the droplet continually spreads over the solid surface until it reaches the steady state. We can clearly see that the contact angle is always changing during the droplet spreading, and finally, the contact angle is approximately equal to its prescribed value  $\theta_s = 45^\circ$ . Figures 6(a) and 6(b) show, respectively, the time evolution of contact-line velocity  $u_{cl}$ , and position  $x_{cl}$  (the  $x$  coordinate of the advancing contact point). Note that  $u_{cl}$  and  $x_{cl}$  are both obtained by the interpolation on the contour of  $\rho^N = 0$ . As shown in Fig. 6(a), at the initial stage of the process, the contact-line velocity increases sharply from zero to the maximum and then continuously decreases until it enters into equilibrium state, at which a zero velocity is reached. From Fig. 6(b) we can observe that the final position of the advancing contact point is  $x_{cl} = 2.287R_0$ , which is close to the theoretical result, i.e.,  $x_{cl} = 2.338R_0$ .

According to Levi *et al.* [32], an exponential power law is observed for the droplet spreading based on experimental data:

$$A^* = 1 - \exp\left(-\frac{K}{A_f}\tau^n\right), \quad (41)$$

in which  $A^*$  is the dimensionless wet area that is defined as the ratio of the instantaneous wet area to the equilibrium wet area, and  $K$  and  $n$  are the fitting parameters determined by physical properties of the droplet and solid surface. Since the droplet is initially in contact with the bottom wall in our 2D simulations, the dimensionless wet area (i.e., the length in 2D cases) is redefined as  $L^* = (L - L_0)/(L_f - L_0)$ , where  $L$ ,  $L_0$ , and  $L_f$  are the instantaneous wet length, initial wet length, and final wet length, respectively. Figure 7 illustrates the time evolution of the dimensionless droplet wet length for three different static contact angles, i.e.,  $\theta_s = 45^\circ$ ,  $60^\circ$ , and  $75^\circ$ . The discrete symbols represent our LBM simulation results, while the solid lines represent the exponential power law, Eq. (41), by fitting to simulation results. The predicted results of Eq. (41) show good agreement with our LBM simulations. Table I gives the

TABLE I. Parameters in Eq. (41) obtained by the best fits of LBM results for various contact angles in the droplet partial wetting process.

$\theta_s$	$K$	$n$	$R^2$	$\theta_s$	$K$	$n$	$R^2$
$35^\circ$	0.351	0.812	0.99863	$65^\circ$	0.262	0.954	0.99985
$40^\circ$	0.310	0.862	0.99922	$70^\circ$	0.261	0.952	0.99981
$45^\circ$	0.288	0.898	0.99958	$75^\circ$	0.258	0.949	0.99976
$50^\circ$	0.276	0.921	0.99976	$80^\circ$	0.254	0.945	0.99971
$55^\circ$	0.269	0.938	0.99985	$85^\circ$	0.247	0.943	0.99964
$60^\circ$	0.266	0.947	0.99986	$90^\circ$	0.241	0.934	0.99958

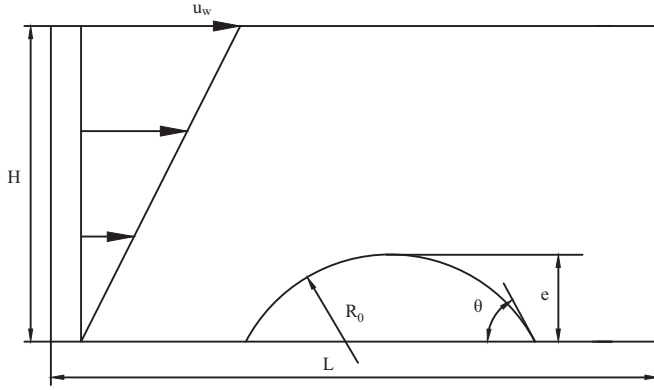


FIG. 8. Schematic diagram of a droplet meniscus subject to a simple shear flow.

values of fitting parameters  $K$  and  $n$ , as well as the correlation coefficients  $R^2$  for the static contact angles ranging from  $35^\circ$  to  $90^\circ$ . Obviously, the values of  $R^2$  are larger than 0.998 for all static contact angles under consideration, indicating that the droplet spreading behavior can be well described by Eq. (41). The values of  $K$  are observed to increase with  $\theta_s$  for the entire range of contact angles, whereas the values of  $n$  increase with  $\theta_s$  for  $\theta_s \leq 65^\circ$  and change slightly when  $\theta_s > 65^\circ$ , which is consistent with the results in Ref. [32].

**B. Droplet subjected to a simple shear flow**

The droplet subjected to a simple shear flow is considered in this section (the geometry setup of this problem is shown in Fig. 8) to test the hysteresis behavior of contact line. We first simulate the droplet remaining static on the solid surface (i.e., the stationary mode thereafter) due to a large hysteresis window, and the obtained results are compared with the previous numerical results. Then we investigate the different modes of droplet motion, namely, stationary, slipping, and breakup modes, which are caused by different Capillary numbers and hysteresis windows.

**1. Droplet pinned on the wall**

We first investigate the cases where the droplet remains pinned on the solid surface due to a large hysteresis window of  $(5^\circ, 175^\circ)$ . At the top surface, the halfway bounce-back

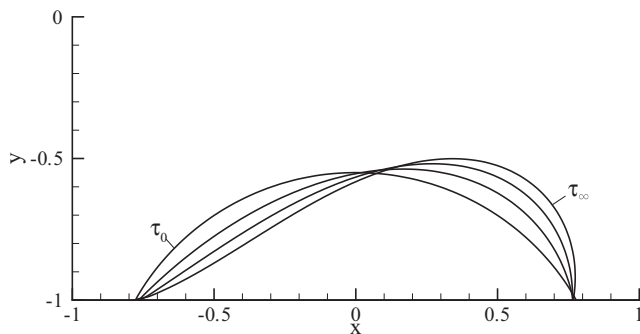


FIG. 9. Time evolution of droplet shape for  $Ca = 0.10$ . Time  $\tau_0$ : initial shape. Time  $\tau_\infty$ : equilibrium shape. The dimensionless time is taken as  $\tau = 0, 11.34, 17.01, 200$ .

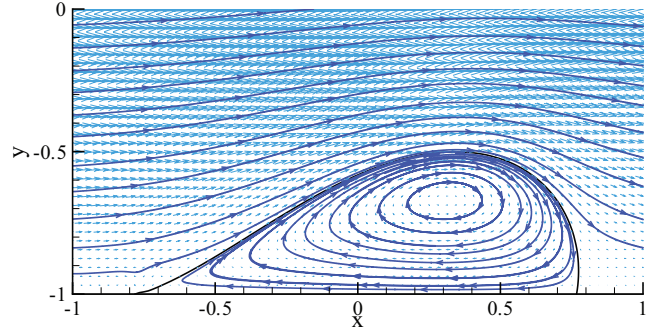


FIG. 10. (Color online) Equilibrium velocity field and streamlines for  $Ca = 0.10$ . The droplet interface is represented by the black solid line.

boundary condition for the moving boundary [33] is used to obtain the wall velocity  $(u_w, 0)$  at the bottom surface; the developed dynamic wetting boundary condition is applied to consider the contact-angle hysteresis; and at both the inlet and outlet, the periodic boundary conditions are used. The physical properties of both fluids are taken as  $\rho_R = \rho_B = 1$ ,  $\nu_R = \nu_B = 0.125$ , and  $\sigma = 0.004$ . Initially, a droplet of circular segment (red fluid) with the radius  $R_0$  and contact angle  $\theta = 60^\circ$  is placed on the bottom wall of a  $L \times H = 512 \times 128$  domain. The problem is characterized by the dimensionless droplet area  $A_d^* = 4A_d/H^2$  and the Capillary number  $Ca = \rho \nu u_w e / (\sigma H)$ .

Figure 9 presents the time evolution of the droplet shape at  $Ca = 0.10$  for moderate droplet size  $A_d^* = 0.5$ . The initial droplet is a symmetric cap, but due to the viscous stresses, it deforms continually toward the flow direction. Once the viscous force acting on the droplet interface is balanced by the interfacial tension, the droplet will reach a steady shape.

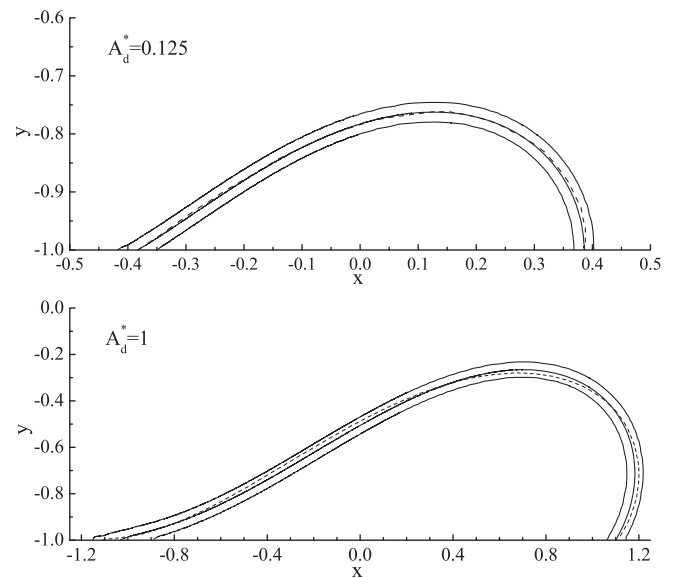


FIG. 11. Comparison of the simulated equilibrium droplet shapes with the shear flow results of Schleizer and Bonnecaze [34] at  $Ca = 0.10$  for  $A_d^* = 0.125$  and 1. The solid lines are the simulated contours at  $\rho^N = \{-0.9, 0, 0.9\}$ , while the dashed lines are the results of Schleizer and Bonnecaze [34].

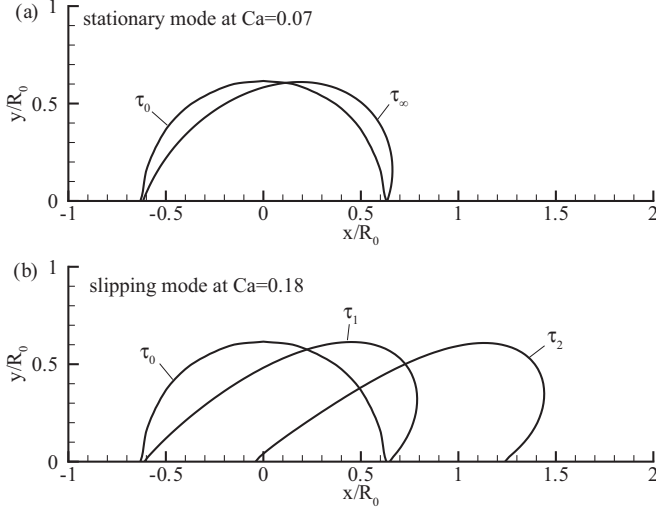


FIG. 12. Evolution of droplet shapes at  $(\theta_R, \theta_A) = (60^\circ, 120^\circ)$  for (a) stationary mode and (b) slipping mode. In (a),  $\tau_0$  denotes initial droplet shape and  $\tau_\infty$  denotes equilibrium shape. In (b),  $\tau_0$  denotes initial droplet shape,  $\tau_1$  denotes the shape at  $\tau = 10.2$  when the droplet starts to move, and  $\tau_2$  is the droplet shape at  $\tau = 76.6$  when the simulation terminates.

Figure 10 presents the velocity field and the streamline of the equilibrium droplet with the same flow condition, and a smooth velocity field with a vortex inside the droplet is observed, which is the typical flow feature of a deformed droplet. Figure 11 compares the predicted equilibrium droplet shapes with the numerical results of Schleizer [34] for dimensionless droplet area  $A_d^* = 0.125$  and  $A_d^* = 1$ . As the droplet size increases, the droplet deforms more significantly to reach a steady shape. For both droplet sizes, the predicted interface profiles ( $\rho^N = 0$ ) agree well with the results of Schleizer and Bonnecaze [34], which indicates good accuracy of our developed model for dealing with hysteresis.

## 2. Droplet motion under a shear flow

Now the deformation and migration of the droplet are investigated at different Capillary numbers and hysteresis windows. The simulations are conducted in a domain of

$200 \times 40$  for a semicircular droplet of radius  $R_0 = 20$  initially placed on the bottom solid surface. The physical properties are taken as  $\rho_R = \rho_B = 1$ ,  $\nu_R = \nu_B = 0.125$ , and  $\sigma = 0.005$ . We use the boundary conditions as described in the last section. We also follow the definition of Capillary number given in the last section, where  $e = R_0$  for the initial semicircular droplet. In the simulations, the Capillary number is varied from 0.01 to 0.3, and the hysteresis window is chosen as  $(90^\circ, 90^\circ)$ ,  $(80^\circ, 100^\circ)$ ,  $(70^\circ, 110^\circ)$ ,  $(60^\circ, 120^\circ)$ , and  $(50^\circ, 130^\circ)$ , which covers a broad range of flow conditions.

When a viscous droplet is subjected to a simple shear flow, the flow pattern of the droplet falls generally into three modes, i.e., stationary, slipping, and breakup modes. Figure 12 presents the time evolution of the droplet shape for stationary and slipping modes at  $(\theta_R, \theta_A) = (60^\circ, 120^\circ)$ . As shown in the figure, at  $Ca = 0.07$ , the droplet is in the stationary mode, where the droplet deforms with time but its contact line remains stationary on the wall; at  $Ca = 0.18$ , the droplet deforms continuously until the receding and advancing contact angles reach the hysteresis limits, and then starts to slip over the wall. Figure 13 illustrates the droplet breakup process at  $Ca = 0.3$  and  $(\theta_R, \theta_A) = (60^\circ, 120^\circ)$ . As the time elapses, the droplet deforms to its limit shape and then breaks up into two separate parts: one moves fast as it breaks away from the solid surface, while the other slips over the solid surface at a relatively small velocity.

Figure 14 presents the relation of Capillary number  $Ca$  and droplet velocity  $u_d$  for different hysteresis windows. The droplet velocity is calculated by

$$u_d = \sum_{i,j} u_x(i,j) N[\rho^N(i,j)] / \sum_{i,j} N[\rho^N(i,j)], \quad (42)$$

in which  $N[\rho^N(i,j)]$  is defined by

$$N[\rho^N(i,j)] = \begin{cases} 0, & \rho^N(i,j) < 0 \\ 1, & \rho^N(i,j) \geq 0 \end{cases} \quad (43)$$

As shown in Fig. 14, for the case without hysteresis, i.e.,  $(\theta_R, \theta_A) = (90^\circ, 90^\circ)$ , the zero velocity is only held at the origin, and no stationary mode is encountered. But in the remaining four hysteresis windows, the left parts of the curves remain nearly overlapped with the abscissa and the stationary

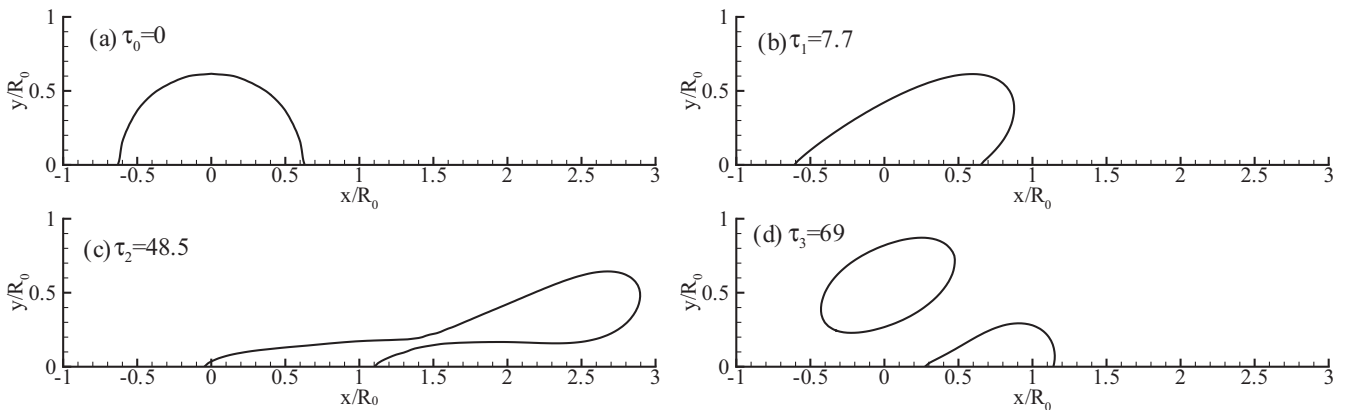


FIG. 13. Evolution of the droplet shape for  $(\theta_R, \theta_A) = (60^\circ, 120^\circ)$  and  $Ca = 0.3$  in breakup mode with the times taken as (a)  $\tau = 0$ , (b)  $\tau = 7.7$ , (c)  $\tau = 48.5$ , and (d)  $\tau = 69$ .

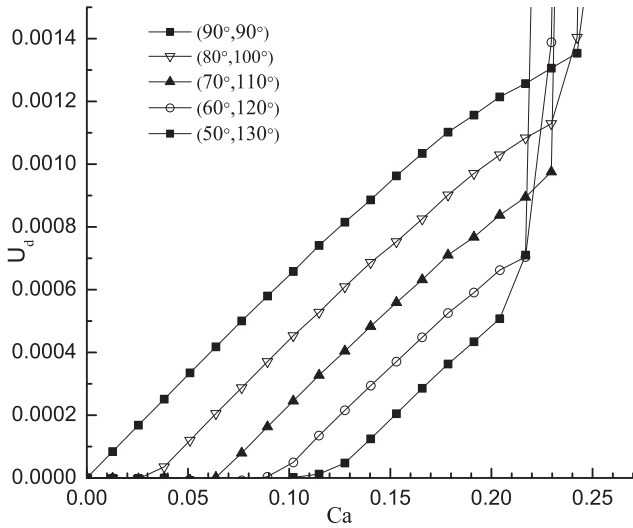


FIG. 14. Droplet velocity as a function of Capillary number for various hysteresis windows.

modes are apparently exhibited. As  $Ca$  increases, the droplet velocity  $u_d$  begins to increase linearly with  $Ca$ , and the droplet enters into the slipping mode for all hysteresis windows. The critical Capillary number (above which the droplet starts to move) increases with the size of hysteresis, since the larger hysteresis corresponds to the larger deformation, and subsequently a larger  $Ca$  is required to move the droplet. For a further increase in  $Ca$ , the droplet motion shifts from the slipping mode to the breakup mode with an abrupt rise of droplet velocity. It is noted that in our simulations, the calculated velocity represents the averaged velocity of the two separated parts of the droplet, and thus, the above-mentioned abrupt rise of velocity in the breakup mode is mainly attributed to the daughter droplet escaping from the solid surface, which moves faster than the bottom one.

In this study, the contact angle is evaluated as the intersection angle of the droplet interface tangent and the wall surface, and the tangent is approximated by the connecting line of

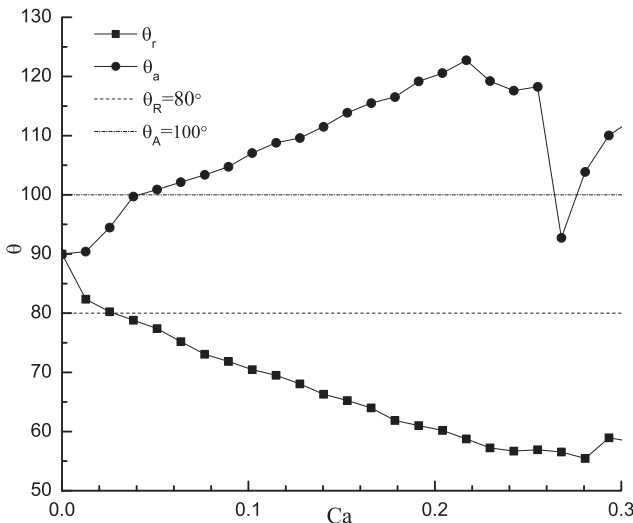


FIG. 15. Receding and advancing contact angles as a function of Capillary number for  $(\theta_R, \theta_A) = (80^\circ, 100^\circ)$ .

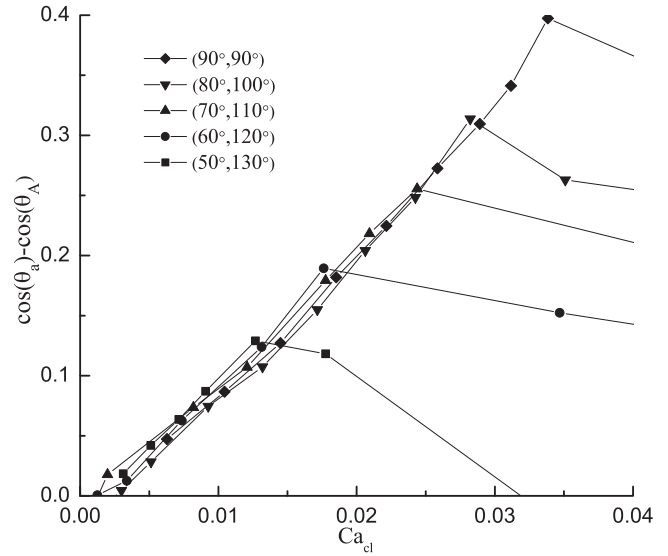


FIG. 16. Relationship between  $(\cos \theta_a - \cos \theta_A)$  and contact-line Capillary number for various hysteresis windows.

two intersection points, which are produced, respectively, by the interface with the wall and the interface with the adjacent grid layer. Figure 15 presents the magnitude of the calculated receding  $\theta_r$  and advancing  $\theta_a$  contact angles against  $Ca$  for the hysteresis window of  $(80^\circ, 100^\circ)$ . As shown in the figures, with an increase in  $Ca$ , the advancing contact angle  $\theta_a$  increases but the receding contact angle  $\theta_r$  decreases, indicating a larger droplet deformation. Beyond the hysteresis window of  $(80^\circ, 100^\circ)$ , both  $\theta_a$  and  $\theta_r$  vary linearly but inversely with  $Ca$  until the droplet breaks up.

Next, we investigate the Navier slip rule between advancing contact angle  $\theta_a$  and the contact-line Capillary number  $Ca_{cl} = \rho \nu u_{cl} / \sigma$  in Fig. 16, in which the contact-line velocity  $u_{cl}$  equals the droplet velocity  $u_d$  for the present shear flow. A linear relation between  $(\cos \theta_a - \cos \theta_A)$  and  $Ca_{cl}$  is approximately exhibited for different hysteresis windows in the slipping mode, which is consistent with the simplified Navier slip rule described by Eq. (40). However, the critical contact-line Capillary number, at which the transition from slipping to breakup occurs, varies for different hysteresis windows owing to the different size of the formed daughter droplets.

Finally, we interestingly investigate the critical values of Capillary number (above which the droplet starts to move) for several different hysteresis windows. As shown in Table II, the Capillary number increases with the hysteresis windows.

TABLE II. Values of Capillary number  $Ca_{cr}$  and  $Ca_{cr} / (\cos \theta_R - \cos \theta_A)$  when the droplet starts to move. Note that the Reynolds and Weber numbers are both negligibly small.

$(\theta_A, \theta_R)$	$Ca_{cr}$	$Ca_{cr} / (\cos \theta_R - \cos \theta_A)$
$(90^\circ, 90^\circ)$	0	
$(80^\circ, 100^\circ)$	0.033	0.0955
$(70^\circ, 110^\circ)$	0.064	0.0932
$(60^\circ, 120^\circ)$	0.093	0.0931
$(50^\circ, 130^\circ)$	0.121	0.0943

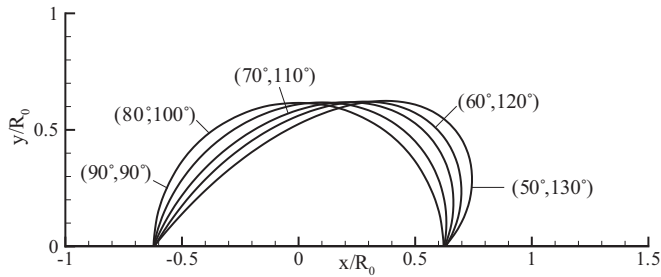


FIG. 17. Critical shapes when the droplet starts to move for different hysteresis windows.

This is because larger hysteresis magnitude leads to the larger deformation to initiate the droplet movement, which is also demonstrated by Fig. 17. Since the Reynolds number and Weber number are both negligibly small for microdroplets in our simulations, the flows are mainly controlled by viscous and capillary forces, which can be a supplement to the simulations in Ref. [27] where inertia and capillary force play a dominant role. A simple force balance between the viscous force ( $\propto \rho \nu u_w e/H$ ) and the capillary force [ $\sigma (\cos \theta_R - \cos \theta_A)$ ] is used to determine the critical flow conditions. This force balance, i.e.,  $Ca_{cr} = \rho \nu u_w e / (\sigma H) \propto (\cos \theta_R - \cos \theta_A)$ , suggests that the critical Capillary number  $Ca_{cr}$  changes proportionally with the hysteresis window ( $\cos \theta_R - \cos \theta_A$ ), corresponding to the small Weber number situation in the simulations of Spelt [35]. Table II presents the values of  $Ca_{cr} / (\cos \theta_R - \cos \theta_A)$  for various hysteresis windows. It is observed that the value of  $Ca_{cr} / (\cos \theta_R - \cos \theta_A)$  is held nearly as a constant for different hysteresis windows, consistent with the prediction from the simple force balance.

#### IV. CONCLUSIONS

A color-gradient-based multiphase LBM is developed to simulate the contact-line dynamics, with particular emphasis on the hysteresis of contact angle. The perturbation operator based on the CSF concept is introduced to model the interfacial tension, and the recoloring algorithm proposed by Latva-Kokko and Rothman [13] is used to maintain the interface and eliminate the lattice pinning problem. At the solid surface, the color-conserving boundary condition [21] is employed to

improve the accuracy of the simulation and suppress spurious velocities at the contact line. A numerical strategy based on an idea of macroscopic contact-angle hysteresis algorithm is introduced to LBM to allow for the effect of hysteresis.

To verify the developed model, numerical simulations are conducted for several typical droplet flows, and the obtained results are compared with the theoretical solutions and experimental data. A brief summary of these studies is given below together with some conclusions.

(1) The developed wetting boundary condition is employed to investigate the equilibrium properties and the dynamic process of a droplet spreading on various partial wetting surfaces. The obtained equilibrium droplet shapes and pressure differences are compared with the analytical solutions, and good agreement is reached. In the dynamic spreading process, the best fits of our simulation results show good agreement with the exponential power law proposed in Lavi *et al.* [32], and the variation trend of  $K$ , and  $n$  with static contact angle  $\theta_s$  is consistent with the experimental results presented in Ref. [32].

(2) The developed model is finally used to simulate the droplet behavior subjected to a simple shear flow. For the droplet pinned on the wall, the predicted shape of deformed droplet agrees well with the result of Schleizer and Bonnecaze [34], which indicates good accuracy of our developed model for dealing with contact-angle hysteresis. Three typical modes of droplet motion (i.e., stationary, slipping, and breakup modes) are well reproduced under different Capillary numbers and hysteresis windows, and the predicted linear relation between the cosine function of the advancing contact angle and the contact-line Capillary number is consistent with the simplified Navier slip rule. Moreover, prediction of the linear relationship between the Capillary number  $Ca_{cr}$  and the hysteresis window ( $\cos \theta_R - \cos \theta_A$ ), which can be derived from the force balance between viscous and capillary forces in the creeping flow, further demonstrates the capability of the developed model for accurately simulating the contact-line motion.

With the present model, the influence of hysteresis on the dynamical behavior of contact line can be studied systematically, which enables us to predict the droplet motion in numerous industrial processes such as immersion lithography, fiber coating, and ink-jet printing, and is also helpful to improve our understanding of the mechanisms controlling the droplet behavior at microscale.

- 
- [1] T. D. Blake, *J. Colloid Interface Sci.* **299**, 1 (2006).
  - [2] C. W. Hirt and B. D. Nichols, *J. Comput. Phys.* **39**, 201 (1981).
  - [3] M. Renardy, Y. Renardy, and J. Li, *J. Comput. Phys.* **171**, 243 (2001).
  - [4] S. Osher and R. Fedkiw, *Level Set Methods and Dynamic Implicit Surfaces* (Springer, New York, 2002).
  - [5] S. Zahedi, K. Gustavsson, and G. Kreiss, *J. Comput. Phys.* **228**, 6361 (2009).
  - [6] K. Kadau, J. L. Barber, T. C. Germann, B. L. Holian, and B. J. Alder, *Philos. Trans. R. Soc. London, Ser. A* **368**, 1547 (2010).
  - [7] C. K. Aidun and J. R. Clausen, *Annual Review of Fluid Mechanics* (Annual Reviews, Palo Alto, 2010), p. 439.
  - [8] H. Liu and Y. Zhang, *J. Comput. Phys.* **229**, 9166 (2010).
  - [9] H. Liu, Y. Zhang, and A. J. Valocchi, *J. Comput. Phys.* **231**, 4433 (2012).
  - [10] X. Shan and H. Chen, *Phys. Rev. E* **47**, 1815 (1993).
  - [11] M. R. Swift, E. Orlandini, W. R. Osborn, and J. M. Yeomans, *Phys. Rev. E* **54**, 5041 (1996).
  - [12] A. K. Gunstensen, D. H. Rothman, S. Zaleski, and G. Zanetti, *Phys. Rev. A* **43**, 4320 (1991).
  - [13] M. Latva-Kokko and D. H. Rothman, *Phys. Rev. E* **71**, 056702 (2005).
  - [14] S. V. Lishchuk, C. M. Care, and I. Halliday, *Phys. Rev. E* **67**, 036701 (2003).

- [15] D. Grunau, S. Y. Chen, and K. Eggert, *Phys. Fluids A* **5**, 2557 (1993).
- [16] T. Reis and T. N. Phillips, *J. Phys. A: Math. Theor.* **40**, 4033 (2007).
- [17] H. Liu, A. J. Valocchi, and Q. Kang, *Phys. Rev. E* **85**, 046309 (2012).
- [18] M. Latva-Kokko and D. H. Rothman, *Phys. Rev. E* **72**, 046701 (2005).
- [19] M. Latva-Kokko and D. H. Rothman, *Phys. Rev. Lett.* **98**, 254503 (2007).
- [20] H. Liu and Y. Zhang, *Phys. Fluids* **23**, 082101 (2011).
- [21] A. P. Hollis, T. J. Spencer, I. Halliday, and C. M. Care, *IMA J. Appl. Math.* **76**, 726 (2011).
- [22] R. G. Cox, *J. Fluid Mech.* **168**, 169 (1986).
- [23] P. Sheng and M. Zhou, *Phys. Rev. A* **45**, 5694 (1992).
- [24] P. G. de Gennes, *Rev. Mod. Phys.* **57**, 827 (1985).
- [25] R. Tadmor, *Langmuir* **20**, 7659 (2004).
- [26] J. K. Park and K. H. Kang, *Phys. Fluids* **24**, 042105 (2012).
- [27] J.-B. Dupont and D. Legendre, *J. Comput. Phys.* **229**, 2453 (2010).
- [28] I. Halliday, A. P. Hollis, and C. M. Care, *Phys. Rev. E* **76**, 026708 (2007).
- [29] Z. Guo, C. Zheng, and B. Shi, *Phys. Rev. E* **65**, 046308 (2002).
- [30] C. D. Cantrell, *Meas. Sci. Technol.* **12**, 2211 (2001).
- [31] P. D. M. Spelt, *J. Comput. Phys.* **207**, 389 (2005).
- [32] B. Lavi and A. Marmur, *Colloids Surf., A* **250**, 409 (2004).
- [33] A. J. C. Ladd, *J. Fluid Mech.* **271**, 285 (1994).
- [34] A. D. Schleizer and R. T. Bonnecaze, *J. Fluid Mech.* **383**, 29 (1999).
- [35] P. D. M. Spelt, *J. Fluid Mech.* **561**, 439 (2006).